Nuclear Instruments and Methods in Physics Research A 1064 (2024) 169381

Contents lists available at ScienceDirect

Nuclear Inst. and Methods in Physics Research, A

journal homepage: www.elsevier.com/locate/nima

Review Article

Cross-talk of a large-scale depleted monolithic active pixel sensor (DMAPS) in 180 nm CMOS technology

Lars Schall [a,*], Christian Bespin [a], Ivan Caicedo [a], Jochen Dingfelder [a], Tomasz Hemperek [a,1], Toko Hirono [a,2], Fabian Hügging [a], Hans Krüger [a], Konstantinos Moustakas [a,3], Heinz Pernegger [b], Petra Riedler [b], Walter Snoeys [b], Norbert Wermes [a], Sinuo Zhang [a]

[a] Physikalisches Institut der Universität Bonn, Nußallee 12, Bonn, Germany
[b] CERN, Espl. des Particules 1, Meyrin, Switzerland

ARTICLE INFO

Keywords:
Pixel detector
Monolithic pixel
CMOS sensor
DMAPS

ABSTRACT

Monolithic pixel detectors combine readout electronics and sensor in a single entity of silicon, which simplifies the production procedure and lowers the material budget compared to conventional hybrid pixel detector concepts. Benefiting from the advances in commercial CMOS processes towards large biasing voltage capabilities and the increasing availability of high-resistivity substrates, depleted monolithic active pixel sensors (DMAPS) can cope with the high-rate and high-radiation environments faced in modern high-energy physics experiments. TJ-Monopix2 is the latest iteration of a DMAPS development line designed in 180 nm TowerSemicondutor technology, which features a large scale $(2\times2)\,\mathrm{cm}^2$ chip divided into (512×512) pixels with a pitch of $(33\times33)\,\mu\mathrm{m}^2$. All in-pixel electronics are separated from its small collection electrode and process modifications are implemented to improve charge collection efficiency especially after irradiation. The latest laboratory measurements and investigations of a periodic variation in the threshold response relative to the hit arrival time observed for TJ-Monopix2 in typical operating conditions are presented.

1. Introduction

The recent advancements in commercial CMOS technologies propel the development of monolithic active pixel sensors (MAPS), which combine readout electronics and sensor in a single piece of silicon [1]. This design approach simplifies the production procedure and reduces the material budget compared to the hybrid pixel detector concept. Additional use of high-resistivity bulk substrates ($\rho > 1\,\mathrm{k\Omega\,cm}$) combined with sufficiently large bias voltage capabilities facilitate the depletion of the sensitive volume and improve the fast charge collection by drift across a pixel [2,3]. Hence, depleted MAPS (DMAPS) have an increased radiation tolerance making them a promising candidate for high-rate and high-radiation environment applications as faced in modern high-energy particle physics experiments. By implementing a small collection electrode relative to the pixel pitch, the in-pixel electronics need to be separated and placed in distinct p-wells. This design approach yields a reduction in sensor capacitance, thereby facilitating both low power consumption and enhanced threshold performance. The long drift distances to the small collection node render the sensor more prone to radiation damage that requires additional process modifications in the sensor layout. The latest prototype of the TJ-Monopix DMAPS development line, TJ-Monopix2, is a large-scale chip designed in 180 nm CMOS technology and high-resistivity substrate. The chip was initially engineered for compliance with the outer layer specifications of the ATLAS Inner Tracker upgrade [4,5]. The observation of a threshold variation relative to the arrival time of hits for TJ-Monopix2 led to an examination trying to identify the cause, magnitude, and possible fixes, which are presented in this contribution.

2. TJ-Monopix2

TJ-Monopix2 is a full scale $(2\times2)\,\mathrm{cm}^2$ DMAPS prototype designed in 180 nm TowerSemiconductor[4] CMOS technology. Based on the ALPIDE pixel detector [6], its small collection electrode relative to the pixel

* Corresponding author.
E-mail address: lars.schall@uni-bonn.de (L. Schall).
[1] Now at: DECTRIS AG, Baden-Dättwil, Switzerland.
[2] Now at: Karlsruher Insitut für Technologie, Karlsruhe, Germany.
[3] Now at: Paul Scherrer Institut, Villingen, Switzerland.
[4] https://towersemi.com/.

https://doi.org/10.1016/j.nima.2024.169381
Received 5 February 2024; Received in revised form 27 March 2024; Accepted 17 April 2024
Available online 19 April 2024

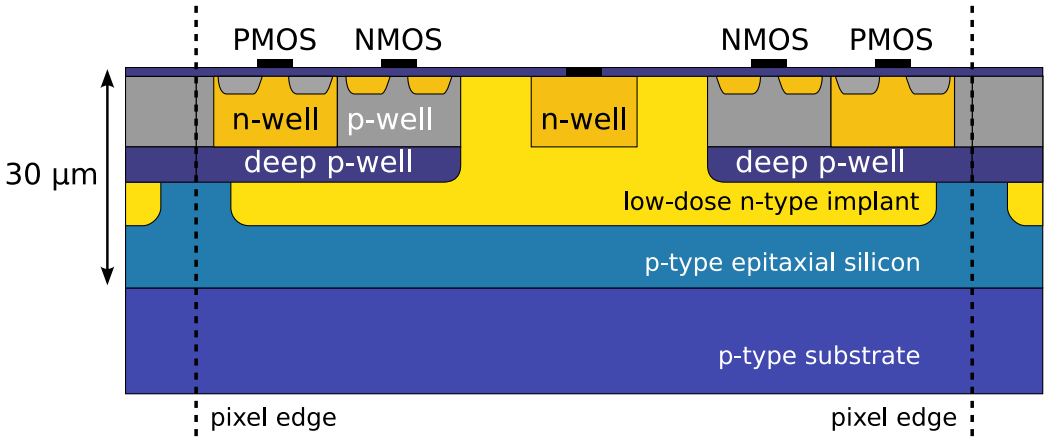

Fig. 1. Schematic cross-section of a single TJ-Monopix2 pixel cell. The low-dose n-implant below the collection electrode facilitates a uniform electric field across the sensor while the gaps in the n-implant layer towards the edges improve the field shaping in the corners of a pixel.

pitch of $(33.04 \times 33.04)\,\mu m^2$ is separated from the in-pixel electronics, which are housed in p-wells at the pixel edges. The sensor capacitance of $\mathcal{O}(3\,fF)$ accomplished by this design approach renders low analog power consumption of ~1 µW and minimal noise operation at ~5 e^-. The extended drift distances to the collection electrode and possible regions with low electric field expose the sensor to an increased probability of charge trapping after irradiation, making the sensor more susceptible to radiation damage. To reach the design target in radiation tolerance of 1×10^{15} $n_{eq}cm^{-2}$ fluence, a low-dose n-implant beneath the collection electrode is implemented to ensure the uniformity of the electric field across the entire sensor [7,8]. Previous studies have shown that an additional modification in the form of a gap in the n-implant is needed to improve the lateral field shaping below the pixel corners after irradiation [9–11]. Fig. 1 shows a schematic cross-section of a single-pixel cell.

TJ-Monopix2 is equipped with the synchronous column-drain readout architecture developed for the FE-I3 readout chip [12]. A 7 −bit gray encoded 40 MHz counter (in the following referred to as BCID counter) is distributed along each double column. Upon a registered hit, the leading and trailing edge (LE/TE) of a discriminated signal is sampled on a pixel level for charge measurements via the time-over-threshold method. The corresponding 40 MHz clock of the BCID counter is internally derived from the 160 MHz command clock in the chip's periphery. Furthermore, each pixel contains a 3 −bit local threshold DAC to minimize the threshold dispersion across the chip. A digital in-pixel injection circuitry is implemented to verify the general functionality of the analog front-end and readout architecture.

3. Observation of a threshold variation

Extensive tests of TJ-Monopix2 have verified improvements in threshold and equivalent noise charge (ENC) performance to its predecessor, TJ-Monopix1, in laboratory conditions [13]. Throughout the characterization, variations in the threshold response of TJ-Monopix2 were observed. To investigate this, the threshold was measured relative to a fixed time of arrival for all hits. The time of injection with respect to the BCID counter was shifted in steps of 3.125 ns by resetting the counter and adding an adjustable delay before every injection. A periodic pattern of the threshold distribution depending on the hit arrival time was observed, which is displayed in Fig. 2 over an exemplary $64 \cdot 25\,ns = 1600\,ns$ interval of the 7 −bit counter. Red markers visualize the average threshold for each measurement point. The measurement was conducted for $\mathcal{O}(30\,000\,pixels)$[5] initially tuned to a mean threshold of 260 e^- with a dispersion of 6 e^-.[6] Within the full BCID counter cycle, a maximum variation in the mean threshold of about 105 e^- was quantified, which exceeds the very good ENC performance of 7 e^- by a factor of 15.

Table 1
Exemplary gray encoding of the first eight BCID counter values. Given the default 40 MHz clock displayed in the first column, the least significant bit toggles at 10 MHz. The toggling frequency is halved for each additional bit.

Time	LE/TE counter	
	Decimal	Gray encoded
0 ns	0	0000
25 ns	1	0001
50 ns	2	0011
75 ns	3	0010
100 ns	4	0110
125 ns	5	0111
150 ns	6	0101
175 ns	7	0100

Beam measurements showed that the most probable value (MPV) of charge created by a minimal ionizing particle (MIP) traversing 30 µm of sensitive sensor material in TJ-Monopix2 is in the order of 2500 e^- [13]. In events where the charge is evenly distributed among four pixels, each pixel is anticipated to collect 625 e^- in charge. The unforeseen threshold variation in the order of 100 e^-, in combination with elevated minimum operating thresholds or diminished total charge collection resulting from radiation damage, could lead to declines in hit detection efficiency relative to the hit arrival time after irradiation.

4. Cross-talk analysis

Extensive tests and investigations of the observed threshold variation were carried out to understand and, if possible, mitigate the underlying effect. Fig. 3 shows a Fourier analysis of the periodic threshold pattern revealing a dominant frequency of 5 MHz and a lesser noticeable 10 MHz component. Due to the gray encoding used in the BCID counter, the observed frequencies are equal to the toggling frequency of the two least significant bits of the counter. Table 1 demonstrates the gray encoded counting method employing the first eight clock cycles, thereby illustrating the resulting toggling frequencies of 10 MHz and 5 MHz.

The simulated transfer function of the pre-amplifier implemented in TJ-Monopix2 is shown in Fig. 4. The highest amplification is achieved

[5] To optimize the total measurement duration, only a fraction of all pixels were activated.

[6] A conversion factor of 8.8 e^- per injected charge DAC unit was applied corresponding to a calibration measurement utilizing Fe55 for this chip.

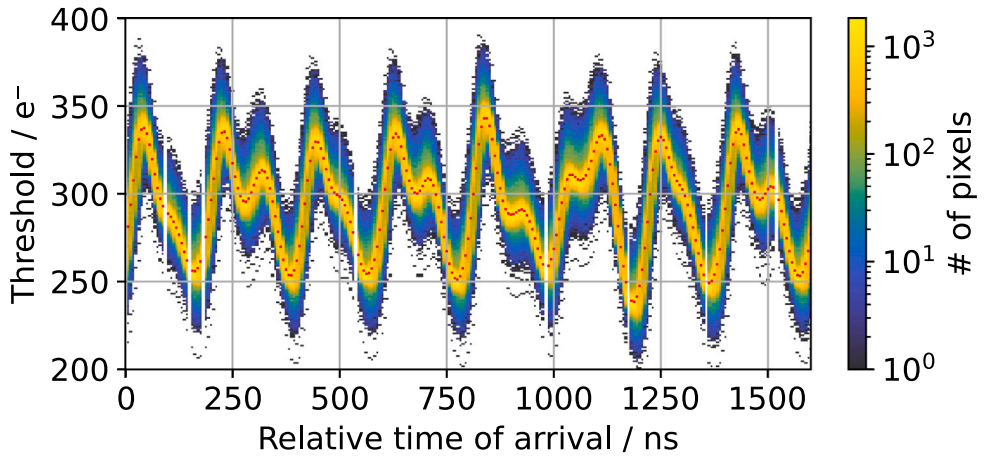

Fig. 2. Tuned threshold distribution for $\mathcal{O}(30\,000\,\text{pixels})$ measured at different relative hit arrival times with respect to the BCID counter running at 40 MHz. The section shown corresponds to half of the 7 −bit full counter resolution. The red dots indicate the average threshold over all activated pixels at each measurement point. A periodic pattern of the threshold response relative to the arrival time of the hits is visible.

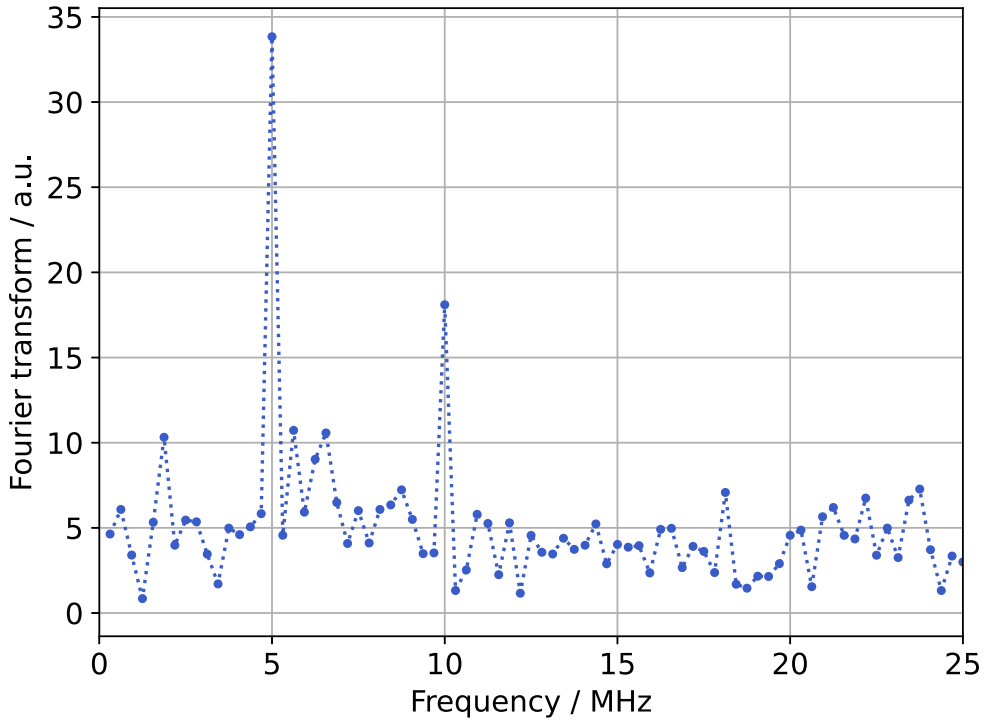

Fig. 3. Fourier analysis of the periodic threshold variation shown in Fig. 2. The analysis reveals a dominant frequency of 5 MHz and a less prominent 10 MHz component.

for signals in the frequency range between 1–10 MHz [14]. Thus, the pre-amplifier facilitates potential cross-talk precisely in the range of frequencies corresponding to the toggling of the BCID counter bits.

Furthermore, a delay in the threshold variation based on pixel position within the matrix was observed, arising from the influence of the BCID counter and injection pulse propagation time. For each pixel, a simple sine function of the form $f(x) = A \cdot \sin(\omega \cdot x + \varphi)$ was fitted to the first two periods of the respective periodic pattern in threshold response. Although the threshold variation only approximates a sinusoidal oscillation, the fit function is still sufficient to quantify the locally dependent propagation delay. The resulting phase parameterization φ was used to approximate the total propagation delay for each pixel, while amplitude A and frequency ω of the fit results were consistent among all pixels. The estimated phase of the threshold variation across the matrix is displayed in Fig. 5. Since the chip periphery and the end of column logic is situated at the bottom of the chip, the observed top-to-bottom gradient in the phase can be explained. This gradient leads to variations in the threshold dispersion relative to the arrival time of hits. Fig. 6 shows the evolution of the threshold dispersion over half of the maximum BCID counter interval. Originating from the combination of threshold variation frequency and phase shift, a periodic pattern in the threshold dispersion is visible. The dispersion reaches up to 20 e^- in case of the most adverse phase difference between the top and bottom pixels, surpassing the initial tuning result of 6 e^- by more than threefold.

Disabling the distribution of the BCID counter across the matrix mitigated the threshold variation completely as shown in Fig. 7. In the absence of leading edge (and charge) information for hits, the

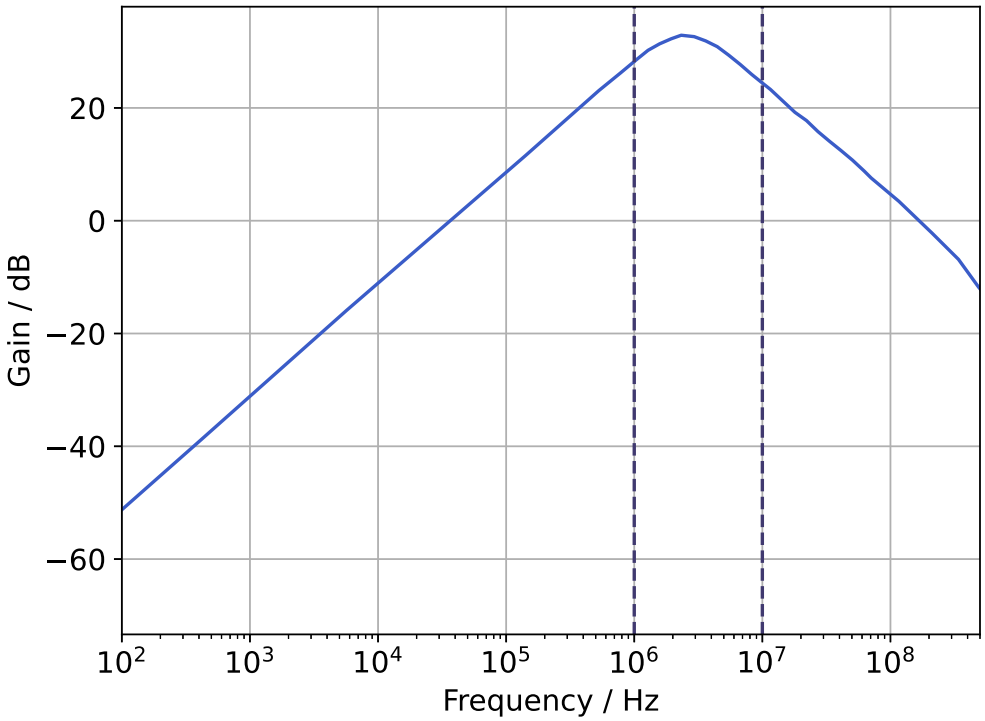

Fig. 4. Simulated transfer function of the pre-amplifier implemented in TJ-Monopix2 (modified from [14]). The dashed lines indicate the range between 1–10 MHz in which the maximum amplification is reached. The exact frequency of the highest gain depends on the exact input capacitance, biasing, and feedback current settings.

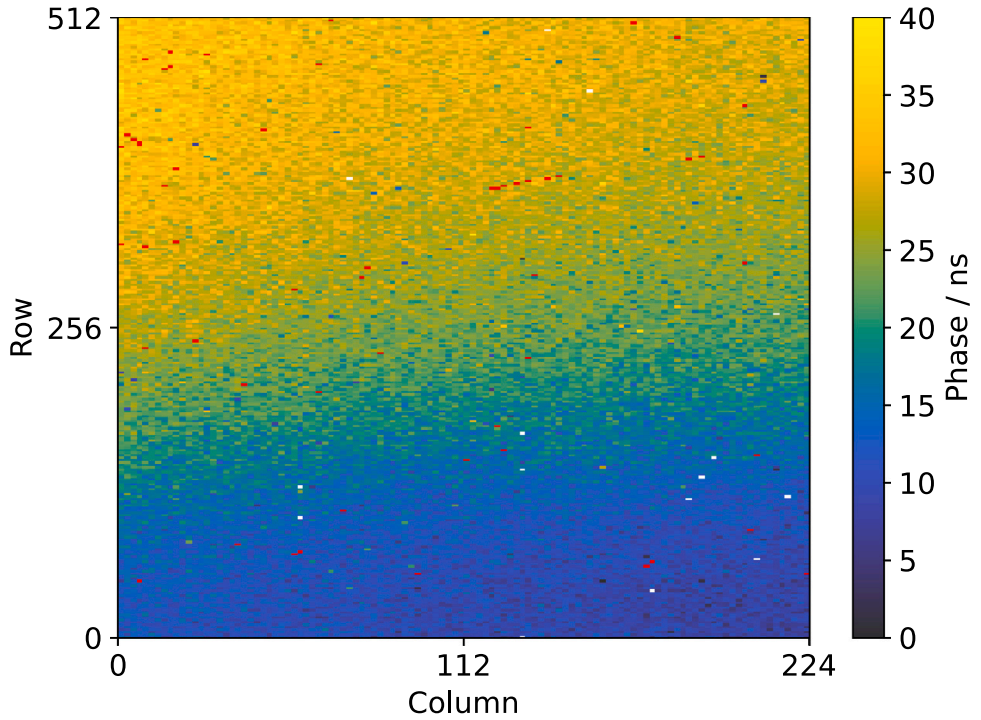

Fig. 5. Per pixel phase estimation of the threshold variation shown in Fig. 2. The phase was quantified by fitting a simple sine function to each pixel's respective periodic threshold variation. Only every fourth pixel in this map was enabled to optimize scan time. The gradient from bottom to top originates from the BCID counter and injection pulse propagation time across the matrix resulting in a local dependency of the threshold variation.

identical assignment of measurement points to a specific time of arrival as previously calibrated is employed. This proves the origin of the cross-talk to arise from the toggling of the BCID counter bits in the matrix.

To better understand which part of the chip is affected by this cross-talk, a measurement with a radioactive source was analyzed for the relative time of arrival of all detected hits. The resulting distribution over the same exemplary segment of the complete BCID counter is shown in Fig. 8. Analog to the observed threshold variation (see Fig. 2), a periodic pattern in the relative hit arrival time of non-injected hits was identified indicating an increased detection rate of hits at periods of lower thresholds. Consequently, this cross-talk does not influence the

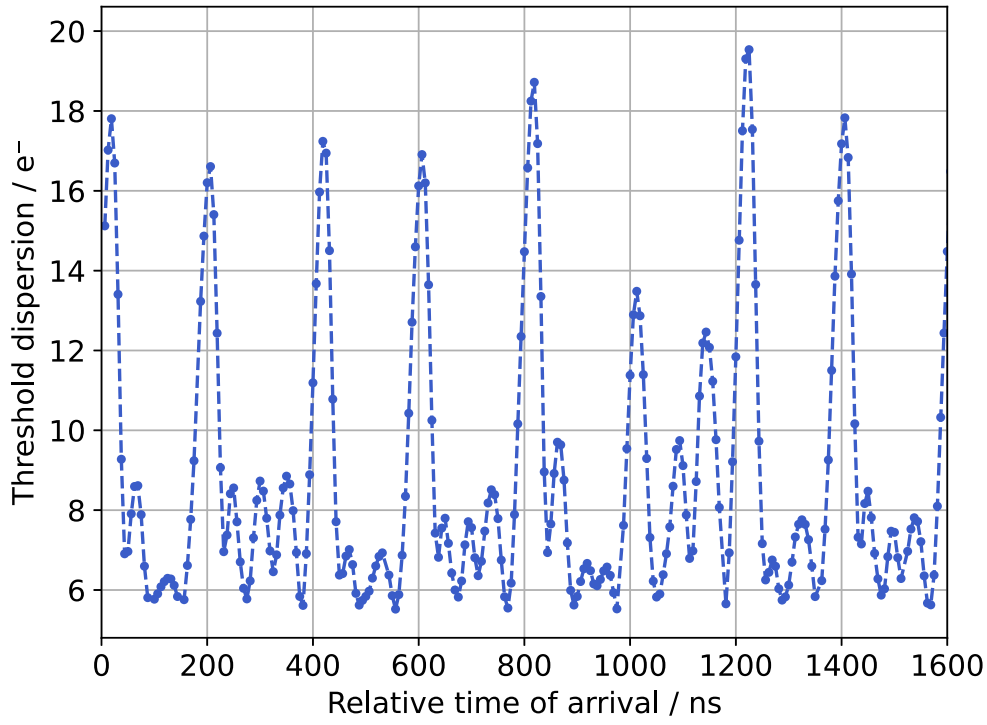

Fig. 6. Threshold dispersion relative to the hit arrival times with respect to the BCID counter. The periodic spikes up to 20 e^- are a direct consequence of the clock and injection propagation time across the matrix as well as the resulting phase difference in the threshold variation.

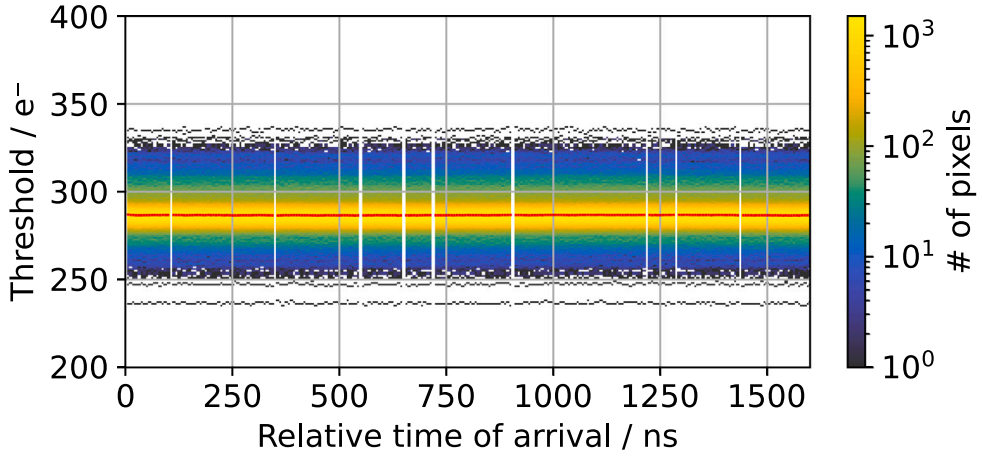

Fig. 7. Variation of the tuned threshold distribution relative to the arrival time of hits for $\mathcal{O}(30\,000$ pixels). Disabling the BCID counter and the corresponding clock significantly reduces the variation and maximum difference in the average threshold across all pixels. The red markers indicate the mean threshold of the activated pixels.

digital injection circuitry, but must impact the measured analog signal of a hit or the threshold level of the chip.

In an attempt to suppress the cross-talk, the internally derived 40 MHz clock was modulated by adjusting the command clock frequency to change the toggling frequency of the BCID counter bits. It was not possible to successfully suppress the threshold variation for a feasible command clock. In case of the deceleration of the clocks by a factor of four (yielding BCID counter bit toggling frequencies of 2.5 MHz and lower), a peak threshold fluctuation of 90 e^- remained. Fourier analysis of the resulting curves resembled the respective change in the toggling frequency of the counter bits within the sensitive pre-amplifier frequency range.

Upon closer investigation of the chip's layout, the responsible distribution lanes of the BCID counter across the matrix were found to be well-shielded. Simulations of the chip's matrix design are currently ongoing to better understand the origin of the observed cross-talk resulting in threshold response variations. For laboratory measurements, a predetermined delay between the reset of the BCID counter and the injection of a hit is used as a practical solution. However, for measurements where the charge information is wanted and the hit arrival times are random relative to the BCID counter, such as beam or radioactive source tests, this approach is not applicable.

The difference in threshold response for laboratory settings with a fixed hit arrival time compared to realistic source or beam measurements is shown in Fig. 9. Both measurements were done using the same chip with identical front-end settings after tuning except for the fixation of the hit arrival time. Since the initial tuning procedure was performed at a (local) minimum in the threshold variation curve, the shift towards larger threshold values was expected. Without fixing the hit arrival time relative to the BCID counter, the measured threshold dispersion increased as hits arrive at the front-end at an arbitrary time and, thus,

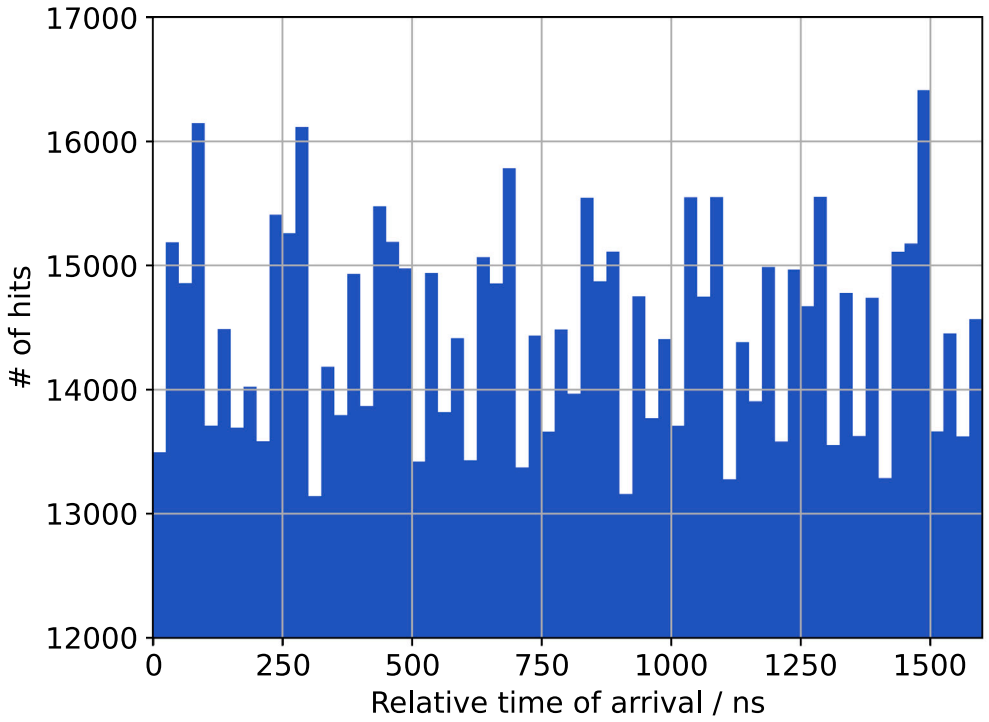

Fig. 8. Relative hit arrival time of a measurement with a radioactive source for an exemplary section of the BCID counter. The periodic pattern analog to Fig. 2 in the relative arrival time of non-injected hits proves that the cross-talk is affecting either the analog signal or the threshold of the chip, but not the injection circuitry.

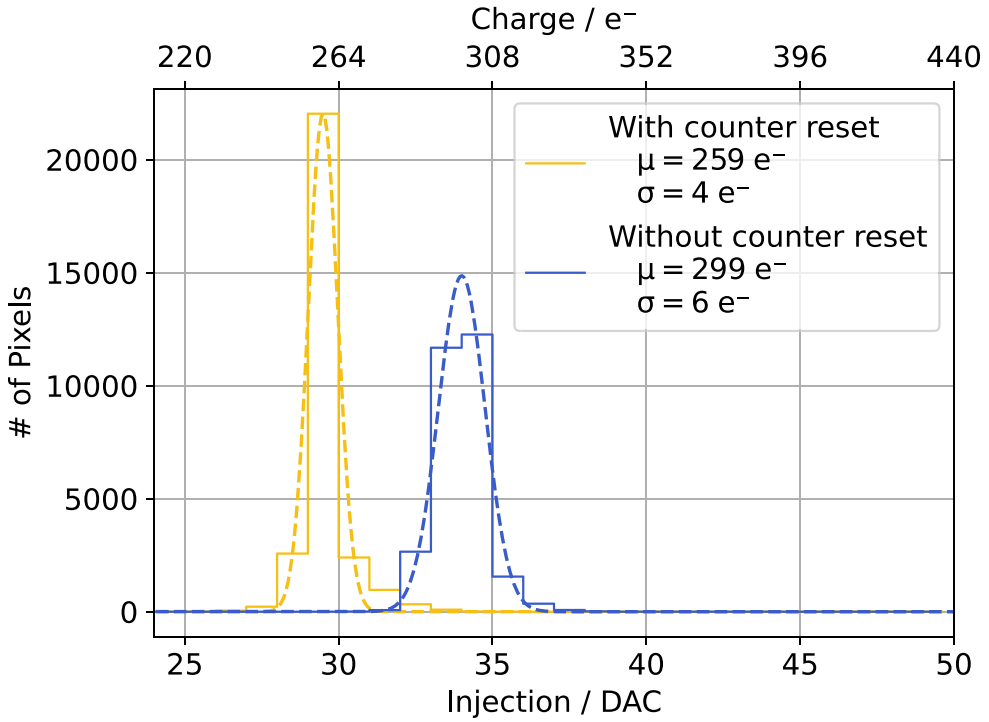

Fig. 9. Comparison of the threshold response with and without resetting the BCID counter for the same chip with identical front-end settings after tuning. The random hit arrival times throughout the scan are responsible for the broadening of the threshold distribution without the reset. The shift towards higher threshold values is explained by the fact that the tuning was performed at a relative hit arrival time corresponding to a (local) minimum of the periodic variation (see Fig. 2). It is important to note that the threshold response without the BCID counter resetting heavily depends on external factors (such as starting the counter-related scan procedure or calculation delays in scripts) and, accordingly, lacks reproducibility.

at a varying threshold. More importantly, this leads to a severe lack of reproducibility of threshold measurements and tuning procedures as well as distortions in charge measurements.

Measured hit-detection efficiencies >99 % of non-irradiated TJ-Monopix2 sensors [13,15] prove the threshold including its variation to be low enough to not affect the beam test performance before

irradiation. However, further investigations are required to quantify the impact of the observed threshold variation on the chip's performance after irradiation to the target fluence of 1×10^{15} $n_{eq}cm^{-2}$. Therefore, irradiated TJ-Monopix2 modules ranging in fluences of 1×10^{14}–1.5×10^{15} $n_{eq}cm^{-2}$ are in preparation and will be tested as soon as they are available. For now, it cannot be excluded that a cross-talk of this magnitude, combined with the degradation in performance due to radiation damage, raises the effective threshold for beam measurements to an extent where losses in the hit detection efficiencies may be observed.

5. Conclusion

The threshold performance of TJ-Monopix2 DMAPS prototypes was further investigated and a modulation of the threshold response relative to the hit arrival time was discovered. A maximum change of $105\,e^-$ in the periodic pattern of the mean threshold was quantified, exceeding the ENC performance of the chip by a factor of 15. Variations in threshold dispersion reaching up to three times the initial value after tuning were measured relative to the hit arrival time and followed the same periodic behavior. Execution of a Fourier analysis on the mean threshold oscillation revealed a dominant 5 MHz frequency, matching the toggling frequency of the second least significant `BCID` counter bit. Analysis of measurements with a radioactive source has shown higher hit detection rates at periods of lower threshold, indicating that the cross-talk affects either the analog signal of a hit or the threshold level of the chip. Mitigation of the threshold variation by disabling the `BCID` counter distribution across the matrix has proven that the cross-talk is caused by the toggling of the counter bits. The constant phase relation between the injection strobe and `BCID` counter, which is typically used for laboratory measurements, hides the observed cross-talk phenomenon. For a better understanding of this behavior, simulations of the chip matrix are still ongoing. In addition, irradiated TJ-Monopix2 modules to fluences up to 1.5×10^{15} $n_{eq}cm^{-2}$ are in preparation which will subsequently be characterized, among other things, for a possible impact of the presented cross-talk on the sensor's performance.

Declaration of competing interest

The authors declare that they have no known competing financial interests or personal relationships that could have appeared to influence the work reported in this paper.

Acknowledgments

This project has received funding from the Deutsche Forschungsgemeinschaft DFG (grant WE 976/4-1), the German Federal Ministry of Education and Research BMBF (grant 05H15PDCA9), and the European Union's Horizon 2020 research and innovation programme under grant agreements no. 675587 (Maria Sklodowska-Curie ITN STREAM), 654168 (AIDA-2020), and 101004761 (AIDAinnova).

References

[1] R. Turchetta, et al., A monolithic active pixel sensor for charged particle tracking and imaging using standard VLSI CMOS technology, Nucl. Instrum. Methods A 458 (2001) 677–689, http://dx.doi.org/10.1016/S0168-9002(00)00893-7.

[2] I. Peric, A novel monolithic pixelated particle detector implemented in high-voltage CMOS technology, in: G. Ambrosi, G.M. Bilei, L. Fano, D. Passeri, A. Santocchia, P. Zuccon (Eds.), Nucl. Instrum. Methods A 582 (2007) 876–885, http://dx.doi.org/10.1016/j.nima.2007.07.115.

[3] M. Barbero, et al., Radiation hard DMAPS pixel sensors in 150 nm CMOS technology for operation at LHC, JINST 15 (05) (2020) 05, http://dx.doi.org/10.1088/1748-0221/15/05/P05013, arXiv:1911.01119.

[4] ATLAS Collaboration, Technical Design Report for the ATLAS Inner Tracker Pixel Detector, Tech. Rep., CERN, Geneva, 2017, http://dx.doi.org/10.17181/CERN.FOZZ.ZP3Q, URL https://cds.cern.ch/record/2285585.

[5] J. Dingfelder, et al., Progress in DMAPS developments and first tests of the Monopix2 chips in 150 nm lfoundry and 180 nm TowerJazz technology, Nucl. Instrum. Methods A 1034 (2022) 166747, http://dx.doi.org/10.1016/j.nima.2022.166747.

[6] M. Mager, ALICE Collaboration, ALPIDE, the monolithic active pixel sensor for the ALICE ITS upgrade, in: M.G. Bisogni, M. Grassi, M. Incagli, R. Paoletti, G. Signorelli (Eds.), Nucl. Instrum. Methods A 824 (2016) 434–438, http://dx.doi.org/10.1016/j.nima.2015.09.057.

[7] W. Snoeys, et al., A process modification for CMOS monolithic active pixel sensors for enhanced depletion, timing performance and radiation tolerance, Nucl. Instrum. Methods A 871 (2017) 90–96, http://dx.doi.org/10.1016/j.nima.2017.07.046.

[8] H. Pernegger, et al., Radiation hard monolithic CMOS sensors with small electrodes for high luminosity LHC, Nucl. Instrum. Methods A 986 (2021) 164381, http://dx.doi.org/10.1016/j.nima.2020.164381.

[9] I. Caicedo, et al., The monopix chips: Depleted monolithic active pixel sensors with a column-drain read-out architecture for the ATLAS Inner Tracker upgrade, JINST 14 (06) (2019) C06006, http://dx.doi.org/10.1088/1748-0221/14/06/C06006.

[10] C. Bespin, et al., DMAPS monopix developments in large and small electrode designs, Nucl. Instrum. Methods A 978 (2020) 164460, http://dx.doi.org/10.1016/j.nima.2020.164460.

[11] M. Dyndal, et al., Mini-MALTA: radiation hard pixel designs for small-electrode monolithic CMOS sensors for the High Luminosity LHC, J. Instrum. (ISSN: 1748-0221) 15 (02) (2020) P02005, http://dx.doi.org/10.1088/1748-0221/15/02/p02005.

[12] I. Peric, et al., The FEI3 readout chip for the ATLAS pixel detector, in: J. Grosse-Knetter, H. Krueger, N. Wermes (Eds.), Nucl. Instrum. Methods A 565 (2006) 178–187, http://dx.doi.org/10.1016/j.nima.2006.05.032.

[13] C. Bespin, et al., Charge collection and efficiency measurements of the TJ-Monopix2 DMAPS in 180 nm CMOS technology, PoS Pixel2022 (2023) 080, http://dx.doi.org/10.22323/1.420.0080.

[14] K. Moustakas, Design and Development of Depleted Monolithic Active Pixel Sensors with Small Collection Electrode for High-Radiation Applications (Ph.D. thesis), Rheinische Friedrich-Wilhelms-Universität Bonn, 2021, URL https://hdl.handle.net/20.500.11811/9315.

[15] M. Schwickardi, et al., Upgrade of Belle II vertex detector with CMOS pixel technology, J. Instrum. 19 (01) (2024) C01054, http://dx.doi.org/10.1088/1748-0221/19/01/C01054.